
Learning Pose Image Manifolds Using Geometry-Preserving GANs and Elasticae

Shenyuan Liang

Department of Statistics
Florida State University
Tallahassee, FL 32306
sl20fu@fsu.edu

Pavan Turaga

School of Electrical Engineering
Arizona State University
Tempe, AZ 85281
pavan.turaga@asu.edu

Anuj Srivastava

Department of Statistics
Florida State University
Tallahassee, FL 32306
anuj@stat.fsu.edu

Abstract

This paper investigates the challenge of learning image manifolds, specifically **pose manifolds**, of 3D objects using limited training data. It proposes a DNN approach to manifold learning and for predicting images of objects for novel, continuous 3D rotations. The approach uses two distinct concepts: (1) **Geometric Style-GAN** (Geom-SGAN), which maps images to low-dimensional latent representations and maintains the (first-order) manifold geometry. That is, it seeks to preserve the pairwise distances between base points and their tangent spaces, and (2) uses Euler’s **elastica** to smoothly interpolate between directed points (points + tangent directions) in the low-dimensional latent space. When mapped back to the larger image space, the resulting interpolations resemble videos of rotating objects. Extensive experiments establish the superiority of this framework in learning paths on rotation manifolds, both visually and quantitatively, relative to state-of-the-art GANs and VAEs.

1 Introduction

Image manifolds are sets of points in image spaces corresponding to images of 3D objects of interest. These manifolds are famously nonlinear, as linear combinations of object images do not always yield plausible images. Learning image manifolds using limited training data is a notoriously difficult problem in computer vision. A specific example is the **rotation or pose manifold**, the set of images of an object under all 3D rotations (while fixing other imaging conditions). Learning a pose manifold can help predict and analyze images of an object from previously unseen poses. One can facilitate simple yet powerful generative and discriminative models for various applications by efficiently re-parameterizing pose manifolds. The potential gains from knowing pose manifolds are enormous.

Problem Specification:

We will follow the framework introduced in [10] to formulate learning of pose manifolds. Let α be a 3D rigid object, such as a chair, airplane, or sportscar, and let O^α denote the object’s 3D geometry and reflectance model. Let $s \in SO(3)$ denote the 3D pose of O^α relative to the camera, and \mathbb{P} represents the orthographic projection of sO^α into the focal plane of the camera, resulting in an image $\mathbb{P}(sO^\alpha)$. As mentioned, all other imaging variables are kept constant for this discussion. Let

the image observation space be $\mathcal{I} = \mathbb{R}^{n \times n}$. The set: $\mathcal{I}^\alpha = \{\mathbb{P}(sO^\alpha) \in \mathbb{R}^{n \times n} | s \in SO(3)\}$, denotes the **rotation or pose manifold** of α . Under assumptions on the smoothness of \mathbb{P} and non-symmetry of O^α with respect to the rotation group, \mathcal{I}^α forms at most a three-dimensional manifold (note that $\dim(SO(3)) = 3$) in the observation space $\mathbb{R}^{n \times n}$.

The problem of learning \mathcal{I}^α can be stated as follows. Given a training set of indexed images $\mathcal{R} = \{(s_i, I_i \equiv \mathbb{P}(s_i O^\alpha)) \in SO(3) \times \mathcal{I}^\alpha, i = 1, 2, \dots, m\}$, our goal is to estimate the full manifold \mathcal{I}^α . (Note that \mathbb{P}, O^α are used in stating the problem but are not available in practice.) More specifically, given an arbitrary rotation $s \in SO(3)$, our goal is to predict the image $\mathbb{P}(sO^\alpha)$ from that viewing angle. Since $SO(3)$ is a closed manifold, the rotation manifold \mathcal{I}^α is also closed, *i.e.*, it has no boundaries. Therefore, if the novel rotation $s \in SO(3)$ lies on a geodesic path $x : [0, 1] \rightarrow SO(3)$ between any two training rotations s_i and s_j , one could use the corresponding image path $t \mapsto \mathbb{P}(x(t)O^\alpha)$ to interpolate between $I_i = \mathbb{P}(s_i O^\alpha)$ and $I_j = \mathbb{P}(s_j O^\alpha)$ and, thus, estimate the desired image. This is possible when \mathbb{P}, O^α are available, but in practice, they are not. Thus, we arrive at the following sub-problem.

Sub-Problem Statement: Given any two training rotations s_i and s_j , and the corresponding images I_i and I_j , find a path between them in the image space that best approximates $t \mapsto \mathbb{P}(x(t)O^\alpha)$, the video of the rotating object. In principle, one can repeatedly apply this solution to estimate new points on \mathcal{I}^α and fill up the whole manifold to address the bigger problem. *In this paper, we focus on this sub-problem.* What is the difficulty in solving this sub-problem? Such learning, especially from sparse data, is challenging for several reasons: (1) Learning nonlinear manifolds in **high-dimensional** spaces typically require a proportionately large number of samples. If the angles s_i, s_j are only a few degrees apart (~ 5 degrees), without a significant change in object appearance, then most image interpolations will work. If the rotations are larger ($\sim 30 - 40$ degrees) apart, one must utilize the underlying manifold geometry. (2) The underlying unknown geometry of \mathcal{I}^α is **complex** and does not follow known patterns such as spheres, ellipsoids, etc. (3) Sparse, isolated data (points) provide **limited geometrical clues**. For example, it is challenging to compute sectional curvatures of \mathcal{I}^α from sparse discrete data.

Our Approach:

Our approach to the estimation of rotation paths $t \mapsto \mathbb{P}(x(t)O^\alpha)$ relies on the knowledge of tangent geometry of \mathcal{I}^α . We use the neighboring training images to learn and estimate tangent spaces of \mathcal{I}^α . Let $s_{i'}$ denote a neighboring rotation of $s_i \in SO(3)$. Then we numerically approximate the tangent vector $v \approx \frac{I_{i'} - I_i}{\theta}$, where θ is the $SO(3)$ distance from $s_{i'}$ to s_i . Using several tangent vectors and SVD, we approximate the tangent space $T_i \equiv T_{I_i}(\mathcal{I}^\alpha)$ at the training point (s_i, I_i) , giving us the pair (I_i, T_i) . With this set up, our approach has two salient steps:

(1) **Geometry-Preserving Dimension Reduction:** We seek a d -dimensional Euclidean latent space and a (computationally invertible) map $\Phi : \mathbb{R}^{n^2} \rightarrow \mathbb{R}^d$ ($d \ll n^2$), such that manifold learning problem is shifted to a smaller manifold: $\mathcal{M}^\alpha \equiv \Phi(\mathcal{I}^\alpha) \subset \mathbb{R}^d$. This learning uses the mapped training set $\{(s_i, (\Phi(I_i), d\Phi(T_i))) \in (SO(3) \times T\mathcal{M}^\alpha), i = 1, 2, \dots, m\}$. Here $d\Phi$ denotes the differential of Φ . This approach raises the question: How to select a Φ that simplifies and facilitates learning the geometry of \mathcal{M}^α ? Instead of using an existing architecture, often designed for a different goal, we design a new GAN that preserves the geometry of \mathcal{I}^α as much as possible. We formulate an objective function that forces Φ to preserve: (1) pairwise Euclidean distances and (2) pairwise tangent space distances on training data when going from image space to the latent space. This approach is in stark contrast with past approaches that force the mapped (latent) spaces to be Euclidean [28, 8].

(2) **Interpolation with Nonlinear Elastica:** The next step is to interpolate between mapped points $\{(\Phi(I_i), d\Phi(T_i))\}$ in the tangent bundle of the smaller space \mathbb{R}^d . Some past papers have imposed an intrinsic Riemannian metric on this space to compute geodesics but with limited success (see next section). Since \mathcal{M}^α is nonlinear and unknown, we use special nonlinear curves, called *free elastica* [24, 21], for this interpolation. Specifically, we use $(\Phi(I_i), d\Phi(T_i))$ at the training points to fit *free elastica* that provide a better interpolation than either straight lines or Riemannian geodesics. The fitted curves are then mapped back to the image space using Φ^{-1} to visualize interpolated paths.

The combination of geometry-preserving mapping Φ and free-elastica interpolation in the latent space makes this approach very different from past efforts in manifold learning.

2 Related Works

In recent years, deep neural networks (DNNs) have provided powerful tools for encoding of images by mapping them to low-dimensional latent spaces. They have received significant attention due to their success in generative modeling. In the following we summarize some past ideas that are most relevant to our method.

GANs: Goodfellow et al. [9] introduced the basic framework and training procedure for GANs. Radford et al. [26] improved the stability and efficiency of GAN training by incorporating strided convolutions in the generator. Karras et al. [14–16] proposed Progressive Growing GAN and Style-Based GAN, which introduces style vectors and perceptual-path-length regularization. More recently, Han et al. [11] addressed the challenges associated with the inverse mapping of Style-Based GANs by training an encoder alongside the generator. However, current GANs primarily focus on producing realistic-looking images rather than on modeling the geometry of the image manifold.

VAEs: Kingma et al. [19] introduced the first VAE where the encoder network maps the input data to a mean and variance vector in the latent space. The decoder maps a random sample from the latent space to the image space. More recently, VAEs have been extended in various directions [27, 7, 5, 6] to improve their performance. For instance, Davidson et al. [6] proposed a Hyperspherical VAE that uses a von Mises-Fisher (vMF) distribution for both the prior and posterior, leading to a hyperspherical latent space. Seeking more generality, Clément et al. [3] modeled the latent space as a Riemannian manifold. The learned metric provides promising results on geodesic interpolations. However, priors in latent space of VAEs are typically predetermined and lack flexibility.

Novel View Synthesis: Several papers in the literature study the task of generating images of objects from novel views, often without estimating geometry of the underlying manifold. For example, Kato et al. [18] proposed a rendering-based approach that uses end-to-end training of the network. Liu et al. [22] improved on this approach by incorporating some simple geometric information into the network. Nguyen et al. proposed a cascaded architecture (RGBD-Net [25]), which consists of a hierarchical depth regression network and a depth-aware generator network. More recently, Jiang et al. [13] explored reconstructing real-world objects from images without known camera poses or object categories. They proposed FORGE framework that can solve shape reconstruction and pose estimation in a unified way. Matthew et al. [31] designed *Neural Radiance Fields* (NerF) to render city-scale scenes spanning multiple blocks. Chattopadhyay et al. [4] presented a graph VAE featuring a structured prior for generating the layout of indoor 3D scenes.

Differential Geometry of Latent Spaces: Bengio et al. [2] stressed the importance of understanding the geometry of latent space representations. Several papers [29, 20, 30] have investigated this geometry and reported them to be (surprisingly) flat. However, these papers mainly utilized *existing* architectures geared towards image synthesis rather than pursuing designs for learning geometries. Arvanitidis et al. [1] studied the geometry of VAEs by imposing a Riemannian metric on the latent space. They also incorporated an emphasis on generated variances in the metric formulation.

3 Proposed Framework: Part 1 – Learning Latent Map Φ

In this section, we introduce the proposed *Geometric Style-GAN* (Geom-SGAN), which aims to preserve the geometry of the image manifold to facilitate learning.

We start with a brief background on StyleGANs and AE-StyleGAN2. Consider a set of images $\{I_i\}_{i=1}^N \in \mathcal{I}$ and corresponding latent vectors $z_i \in \mathcal{Z} \equiv \mathbb{R}^d$, $i = 1, \dots, N$, sampled from a probability distribution \mathcal{P}_z . StyleGANs (15–17) use a *Multilayer perceptron* (MLP) mapping network, denoted as $F : \mathcal{Z} \rightarrow \mathcal{W}$, to map z_i into an intermediate latent space $w_i \in \mathcal{W}$, which is then fed to a generator $G : \mathcal{W} \rightarrow \mathcal{I}$ that synthesizes an image $G(F(z_i))$. The discriminator Q distinguishes between real and generated images. The adversarial objective function of StyleGANs is formulated as $\min_G \max_D \left(\mathbb{E}_I [\log Q(I)] + \mathbb{E}_{z \sim \mathcal{P}_z} [\log(1 - Q(G(F(z))))] \right)$. StyleGANs introduce a disentangled latent space \mathcal{W} that enables control of specific image features, thereby providing a versatile model for high-quality image generation. However, a major drawback of StyleGAN architecture is the difficulty of learning the inverse mapping $\mathcal{I} \rightarrow \mathcal{W}$, which poses a challenge to understanding the image synthesis process.

The architecture of VAEs [19, 27, 7, 5, 3] is widely recognized to produce highly effective inversion reconstruction, achieved by the encoder $E : \mathcal{I} \rightarrow \mathcal{W}$, which is trained in conjunction with the generator G . Nevertheless, the disentanglement of the latent space of VAEs is often compromised due to the absence of adversarial loss. To address these limitations, Han et al. [11] introduced a novel training procedure called AE-StyleGAN2, which involves training an encoder E alongside the generator G in StyleGAN2 [16] with an adversarial loss. Readers are referred to the original papers [16, 11] for details of the network architecture and training algorithm.

3.1 Geom-SGAN for geometry preservation

Despite its success in disentangling latent space and inverting reconstructions, AE-StyleGAN2 [11] does not consider the geometry of the underlying image manifold. Indeed it uses *Frechet Inception Distance* (FID) [12] and *Learned Perceptual Image Patch Similarity* (LPIPS) as evaluation metrics that are often used for assessing image quality but do not capture any geometry. For preserving geometry, we propose Geom-SGAN, which starts by compressing the high dimensional image space into an intermediate *Principal Component Analysis* (PCA) space, represented by the mapping $P : \mathcal{I} \rightarrow \mathcal{I}^p$. Accordingly, we formulate a novel, end-to-end objective function based on pairwise Euclidean distances and pair-wise tangent space distances into the Encoder (E) and Generator (G) networks in AE-StyleGAN2. Our proposed framework develops a Φ and its inverse Φ^{-1} , where $\Phi = E \circ P$ and $\Phi^{-1} = P^{-1} \circ G$, respectively, and where the symbol \circ denotes function composition. We describe this construction in more detail next. A schematic of the training and inference procedure is laid out in Fig. 1.

PCA: Linear dimension reduction technique for image pre-processing: An initial step in the mapping is a PCA-based linear dimension-reduction of the training images. Consider a collection of images $\{I_i \in \mathbb{R}^{c \times H \times L}\}_{i=1}^N$, where c , H , and L represent the number of channels, image width, and image height, respectively. By applying PCA, denoted as $P : \mathbb{R}^{c \times H \times L} \rightarrow \mathbb{R}^{c \times h \times l}$, we get a reduced representation of training images, represented by $\{I_i^p \in \mathbb{R}^{c \times h \times l}\}_{i=1}^N$. Notably, during the PCA reconstruction stage, we employ a denoising network consisting of several convolutional layers followed by residual blocks. The objective of the denoising network is to eliminate potential background artifacts introduced in PCA reconstruction.

3.1.1 Preserving Pair-wise Euclidean Distances

One of the training objective is to ensure that close points in image space are also close in latent space, and vice versa.

To train and optimize the generator G , we start by sampling a large batch of latent vectors $z \in \mathbb{R}^{b \times d}$ from standard multivariate Gaussian distribution and use a MLP network $F : \mathbb{R}^{b \times d} \rightarrow \mathbb{R}^{b \times d}$ to map z to the intermediate latent vector $w = F(z)$, where b, d represents the batch size and dimension of the latent vectors, respectively. We then calculate the pair-wise Euclidean distance matrix $D^w \in \mathbb{R}^{b \times b}$ (Line 3 in Algorithm 1) in this w space. The intermediate latent vectors w are further fed into the generator G , producing a batch of fake images $\tilde{I}^p = G(w) \in \mathbb{R}^{b \times c \times h \times l}$. We also compute the pair-wise Euclidean distance matrix $D^{\tilde{I}^p} \in \mathbb{R}^{b \times b}$ (Line 4 in Algorithm 1) with respect to \tilde{I}^p . The loss function for preserving pairwise distances is defined to be:

$$l_d(D^w, D^{\tilde{I}^p}) = \mathbf{1}_b - \sum_{k=1}^b \frac{(D_k^w - \mu^w) \cdot (D_k^{\tilde{I}^p} - \mu^{\tilde{I}^p})}{\|D_k^w - \mu^w\| \|D_k^{\tilde{I}^p} - \mu^{\tilde{I}^p}\|} \quad (1)$$

where $D_k^w, D_k^{\tilde{I}^p} \in \mathbb{R}^b$, $\mathbf{1}_b \in \mathbb{R}^b$ is a vector of ones, $\mu^w, \mu^{\tilde{I}^p} \in \mathbb{R}^b$ are the row-wise mean of D^w and $D^{\tilde{I}^p}$, $\|\cdot\|$ is the Euclidean norm, and \cdot is the Hadamard product.

The encoder E is optimized in a similar fashion. See Algorithm 1 in supplementary material.

3.1.2 Preserving Pair-wise Tangent Space Distances

The second training objective to maintain pair-wise distances (or angles) between tangent spaces when we map images into latent vectors. This is crucial for ensuring that geometry of the image manifold is preserved during the generation and inversion process.

Algorithm 1 Pair-wise distance condition for optimizing generator G .

- 1: Given F and G .
 - 2: Sample $z \in \mathbb{R}^{b \times d}$ from the standard Multivariate Gaussian Distribution.
 - 3: $w = F(z) \in \mathbb{R}^{b \times d}$, $D_{k,m}^w = \|w_k - w_m\|$, where $k, m = 1, \dots, b$, $w_k, w_m \in \mathbb{R}^d$.
 - 4: $\tilde{I}^p = G(w)$, $D_{k,m}^{\tilde{I}^p} = \|\text{vec}(\tilde{I}_k^p) - \text{vec}(\tilde{I}_m^p)\|$, where $\tilde{I}_k^p, \tilde{I}_m^p \in \mathbb{R}^{c \times h \times l}$.
 - 5: Compute $l_d(D_w, D_{\tilde{I}^p})$, where l_d is defined in Eqn. 1 and do backpropagation.
 - 6: Update the weights in G .
-

For optimizing generator G , we start by sampling a large batch of latent vectors $z \in \mathbb{R}^{b \times d}$ from standard multivariate Gaussian distribution and use the MLP network $F : \mathbb{R}^{b \times d} \rightarrow \mathbb{R}^{b \times d}$ to map z to the intermediate latent vector $w = F(z)$. Then for each $w_k \in \mathbb{R}^d, k = 1, \dots, b$ in the batch, we determine its neighbors using Euclidean distances and combine a w_k with its neighbors to form a larger matrix W' of size $\mathbb{R}^{b \times n' \times d}$, where n' is the number of neighbors selected for each w_k in the batch. We further expand $w \in \mathbb{R}^{b \times d}$ to $W^* \in \mathbb{R}^{b \times n' \times d}$, where each of the n' columns is a replicate of w . The tangent plane in latent space is then approximated as $T^w = W' - W^*$ and the projection matrix is computed as $\mathcal{P}^{T^w} \in \mathbb{R}^{b \times d \times d}$ (Line 6 in Algorithm 2). Based on the projection matrix, we can compute the pair-wise distance matrix $D^{T^w} \in \mathbb{R}^{b \times b}$ for T^w (Line 7 in Algorithm 2). The intermediate latent vector with its neighbors, denoted as W' , is further fed into the generator (G), producing a batch of fake images denoted as $I^p = G(W') \in \mathbb{R}^{b \times n' \times c \times h \times l}$. Besides, we also expand $\tilde{I}^p \in \mathbb{R}^{b \times c \times h \times l}$ to $I^{*p} \in \mathbb{R}^{b \times n' \times c \times h \times l}$, where $\tilde{I}^p = G(w)$ and each of the n' columns is a replicate of \tilde{I}^p . The tangent plane in image space is then constructed as $T^{\tilde{I}^p} = I^p - I^{*p}$, and the projection matrix is computed as $\mathcal{P}^{T^{\tilde{I}^p}} \in \mathbb{R}^{b \times chl \times chl}$ (Line 10 in Algorithm 2). Based on the projection matrix, we compute the pair-wise distance matrix $D^{T^{\tilde{I}^p}} \in \mathbb{R}^{b \times b}$ for $T^{\tilde{I}^p}$ (Line 11 in Algorithm 2). The expression for the loss function l_d is same as in Eqn. 1 but with the terms $D^{T^{\tilde{I}^p}}, D^{T^w}$.

The encoder E is optimized in a similar fashion. See Algorithm 2 in the supplementary material.

Algorithm 2 Pair-wise tangent space distances condition for optimizing generator G .

- 1: Given F and G .
 - 2: Sample $z \in \mathbb{R}^{b \times d}$ from the standard Multivariate Gaussian Distribution.
 - 3: $w = F(z) \in \mathbb{R}^{b \times d}$. Then for each $w_k \in \mathbb{R}^d, k = 1, \dots, b$, find its n' nearest neighbors based on Euclidean norm, then stack the resulting neighbors onto w , which yields a larger matrix denoted as $W' \in \mathbb{R}^{b \times n' \times d}$.
 - 4: Expand w to $W^* \in \mathbb{R}^{b \times n' \times d}$, where each of the n' columns is a replicate of w .
 - 5: Construct tangent plane in latent space as $T^w = W' - W^*$.
 - 6: Compute projection matrix for tangent plane T^w as $\mathcal{P}_k^{T^w} = (T_k^w)^T T_k^w$, where $k = 1, \dots, b$, and $T_k^w \in \mathbb{R}^{n' \times d}$.
 - 7: Compute pair-wise distance matrix $D_{k,m}^{T^w} = \|\mathcal{P}_k^{T^w} - \mathcal{P}_m^{T^w}\|_f$, where $k, m = 1, \dots, b$, $\mathcal{P}_k^{T^w}, \mathcal{P}_m^{T^w} \in \mathbb{R}^{d \times d}$, and $\|\cdot\|_f$ is the Frobenius Norm.
 - 8: $\tilde{I}^p = G(w) \in \mathbb{R}^{b \times c \times h \times l}$, $I^p = G(W') \in \mathbb{R}^{b \times n' \times c \times h \times l}$. Then expand \tilde{I}^p to $I^{*p} \in \mathbb{R}^{b \times n' \times c \times h \times l}$, where each of the n' columns is a replicate of \tilde{I}^p .
 - 9: Construct tangent plane in image space as $T^{\tilde{I}^p} = I^p - I^{*p}$.
 - 10: Reshape the size of $T^{\tilde{I}^p}$ from $\mathbb{R}^{b \times n' \times c \times h \times l}$ to $\mathbb{R}^{b \times n' \times chl}$, and compute the projection matrix for tangent plane $T^{\tilde{I}^p}$ as $\mathcal{P}_k^{T^{\tilde{I}^p}} = (T_k^{\tilde{I}^p})^T T_k^{\tilde{I}^p}$, where $k = 1, \dots, b$, and $T_k^{\tilde{I}^p} \in \mathbb{R}^{n' \times chl}$.
 - 11: Compute pair-wise distance matrix $D_{k,m}^{T^{\tilde{I}^p}} = \|\mathcal{P}_k^{T^{\tilde{I}^p}} - \mathcal{P}_m^{T^{\tilde{I}^p}}\|_f$, where $k, m = 1, \dots, b$, $\mathcal{P}_k^{T^{\tilde{I}^p}}, \mathcal{P}_m^{T^{\tilde{I}^p}} \in \mathbb{R}^{chl \times chl}$.
 - 12: Compute $l_d(D^{T^{\tilde{I}^p}}, D^{T^w})$, where l_d is defined in Eqn. 1 and do backpropagation.
 - 13: Update the weights in G .
-

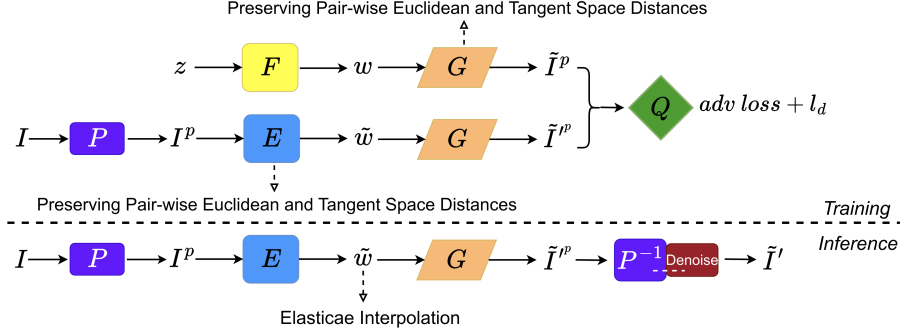


Figure 1: Training procedure. Our method constrains the generator (G) and the encoder (E), with a loss function l_d defined in Eqn. 1, to preserve the local geometry of image space.

3.2 Implementation Details

Experiments are conducted on a Linux workstation with Nvidia RTX 3090 (24GB) GPU and AMD Ryzen 3900x CPU @ 4.6GHz with 64GB RAM. The hyperparameters of generator G , MLP F are chosen to be identical to those in paper [16], Similarly, The hyperparameter of encoder E is chosen to be the same as in paper [11]. The image size $c \times H \times L$ of training and testing set is $3 \times 128 \times 128$, and the reduced images size $c \times h \times l$ after PCA is $3 \times 16 \times 16$. The dimension d of latent space \mathcal{W} is 8. During the training, the batch size b is set to 128, and the number of neighbors n' selected to preserve Pair-wise Tangent Space Distances is 12.

4 Proposed Framework: Part 2 – Elasticae Interpolation

Elastica are smooth, nonlinear curves that can be used to interpolate between directed points, *i.e.*, Euclidean points and attached tangent vectors. Let w_1, w_2 be given two points in the intermediate latent space of Geom-SGAN, and let \tilde{T}_1, \tilde{T}_2 be the corresponding tangent planes. First we find vectors $v_1 \in \tilde{T}_1$ and $v_2 \in \tilde{T}_2$ that are pointing most towards each other, *i.e.*, the Euclidean inner product is as close to -1 . Then, we seek to interpolate between the directed points (w_1, v_1) and (w_2, v_2) and we will do so using elastica.

We briefly introduce the concept of elastica. Let \mathcal{C} be the set of all parameterized, smooth curves in \mathbb{R}^d . For an $\eta \in \mathcal{C}$, let $\dot{\eta}$ and κ_η denote its velocity vector and (scalar) curvature functions. Define $E[\alpha] = \frac{1}{2} \int_0^1 \kappa_\eta^2(s) ds$ to be the elastic energy of η .

Definition 1. A (fixed-length) elastica is defined as an optimal curve according to: $\hat{\eta} = \arg \min_{\eta \in \mathcal{C}} E[\eta]$, such that $\eta(0) = w_1$, $\eta(1) = w_2$, $\dot{\eta}(0) = v_1$, $\dot{\eta}(1) = v_2$, and $length(\eta) = L$.

A physical interpretation of $\hat{\eta}$ is that it provides the smoothest interpolation of a directed point (w_1, v_1) into another (w_2, v_2) with a curve of length L . Since we do not know the length L beforehand, we pursue a modified solution that minimizes $(E[\eta] + \lambda L[\eta])$, where $\lambda > 0$ is a constant. A higher λ constraints the solutions to be smaller curves with high elastic energy and vice versa. These solutions are called *free elastica*. Mumford [24] advocated the use of free-elastica as the most likely solutions to fill in the missing or obscured curves in images, *e.g.* in the famous Kanizsa triangles. Mio et al. [23] provided computationally efficient procedures for computing these different elastica in arbitrary Euclidean spaces. We refer the reader to Algorithm 4.2 in [23] for details. Fig. 2 shows two examples of interpolating between directed points in \mathbb{R}^3 for several values of λ . The rightmost panel shows effects of noisy directions on the resulting elastica (for a fixed λ).

In our experiments, we use $\lambda = 1$ to compute free elastica. We map these interpolated paths back to the image space as $\Phi^{-1}(\eta(t))$ and visualize them as sequences of images. Fig. 3 shows an illustration of the final result. It uses two images of a chair corresponding to two different pose, and uses this framework to interpolate a path. The fourth row in Fig. 3 shows images at nine equally-spaced points on this path. The other rows in this figure use interpolations in latent spaces of some other recent frameworks (listed in the next section). Fig. 4 in the supplementary presents more examples.

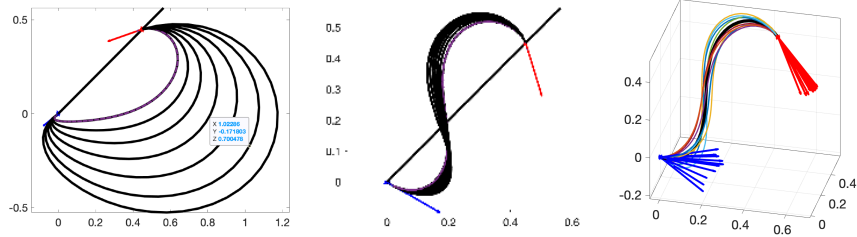


Figure 2: Left and middle: Examples of free elastica between directed points for different length penalties. Right: Analysis of stability of elastica wrt noise in tangent directions.

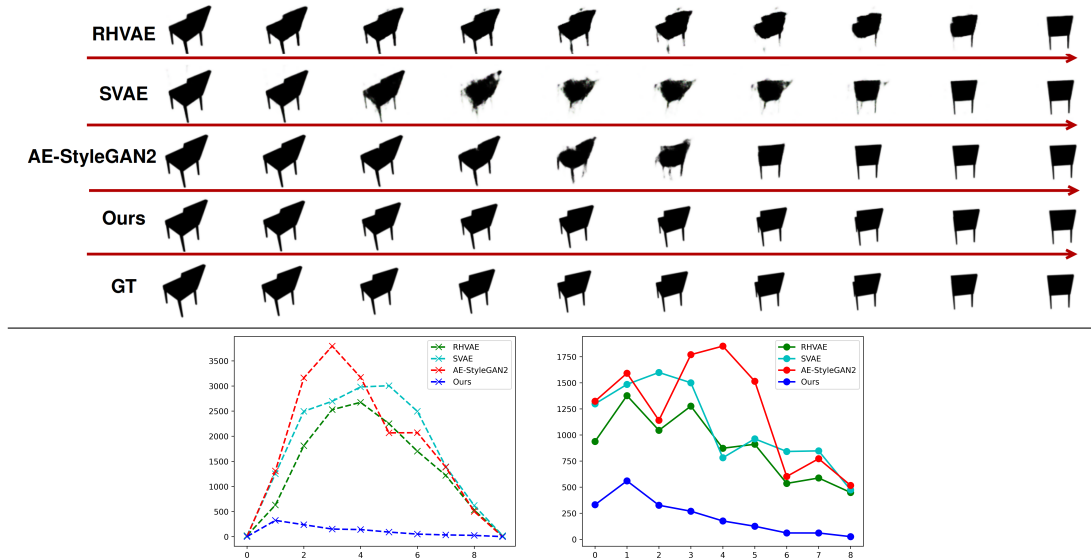


Figure 3: Top: Each row shows an interpolated path between the original pose (leftmost) and the rotated pose (rightmost) using the corresponding methods. The rotation angle between the two pose is 40 degrees. Bottom: Plots of time-indexed squared errors in the image space (left) and the tangents (right) for different methods.

5 Experiments

In this section, we present the results from our experiments. The results are compared against *Riemannian Hamiltonian VAE* (RHVAE) [3], *Hyperspherical VAE* (SVAE) [6], and AE-StyleGAN2 [11] for a comprehensive evaluation.

5.1 Experimental Setup

Data: In order to evaluate the efficacy of our proposed methodology, we use synthetic datasets for four objects, namely chair, plane, sports car and teapot. Each dataset consists of RGB images captured from a **3D object** that has been rotated along its x, y, and z axes with angle increments of up to 180 degrees. The **training set** consists of 1200 RGB images that are sparsely captured from evenly spaced angles, while the **testing set** consists of 3600 RGB images densely sampled from different angles within the same range as the training set. The images in the test set do not overlap with the angles in the training set. Both the training and testing images are 128×128 pixels with 3 color channels.

Evaluation metrics: We compare interpolations resulting from different methods with the ground truth paths since we have the ground truth available. We consider interpolations for rotations ranging

from 15 to 40 degrees, as this interval represents a challenging and informative subset of the possible rotations. We assess the performance of our proposed approach and the other SOTA methods through both quantitative and qualitative evaluations.

For **quantitative comparisons**, we use two metrics. Let $\{I'^t \in \mathbb{R}^{c \times H \times L}\}_{t=1}^T$ denote an interpolated path (indexed by t) and $\{I^t \in \mathbb{R}^{c \times H \times L}\}_{t=1}^T$ be the ground truth path (also indexed by t). Firstly, we compute the *Squared Error* (SE) between the I'^t and I^t , defined as $\|I'^t - I^t\|^2$. This criterion provides a numerical measure of the accuracy of these methods and allows us to objectively compare their performances. Secondly, we compare the velocity vectors along the inferred paths between the estimated and the ground truths. A velocity vector is computed using temporal differences, and the error is defined using $E_v^t = \|I'^{(t+1)} - I'^t - (I^{(t+1)} - I^t)\|^2$. This compares the inferred paths with the ground truth in terms of the tangent vectors. For **qualitative comparisons**, we visualize the constructed paths and compare them to the ground truth rotation paths.

5.2 Evaluation Results

As mentioned, we compare our method with three recent deep-learning generative models: **1. RHVAE** [3] is a geometry-based VAE that models the latent space as a Riemannian manifold. The method combines Riemannian metric learning and normalizing flows, which are used for geodesic shooting. **2. SVAE** [6] samples latent vectors from von Mises-Fisher (vMF) distribution and use spherical linear interpolation to derive geodesics. **3. AE-StyleGAN2** [11] introduced a novel training procedure that involves training an encoder and a Style-based generator jointly with a shared discriminator. The proposed approach results in a more disentangled latent space and achieves better inversion reconstruction than StyleGAN2.

Qualitative comparison. We show examples of interpolated paths obtained with different methods for different objects in Fig. 3 and Fig. 4. The results are drawn row-wise: in each row, we show an interpolated path between the original and rotated objects. ([Additional examples are provided in the supplementary material](#)). We can see that the interpolated paths obtained by our method are close to the ground truth, while the other methods severely distort intermediate images in multiple ways.

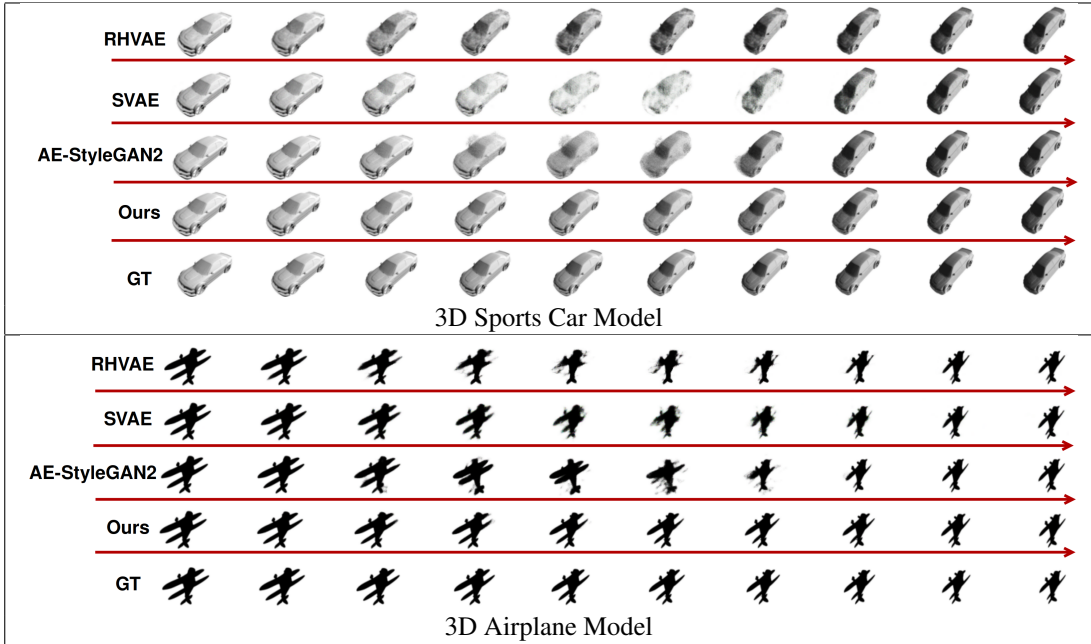


Figure 4: Visualization of interpolated path for a 3D Sports Car and Airplane models. Each row shows an interpolated path between the original object image and the rotated object image. Error quantifications are presented in Fig. 5.

Quantitative comparison. For each test object: chair, sports car, and airplane, we compute 114 different rotation paths by taking arbitrary rotation pairs in the test data, with rotation angles ranging from 15 to 40 degrees. We sample these paths at eight intermediate samples indexed by t . For each time index t , we calculate summary statistics of the two SEs mentioned above – image SE and tangent SE. Naturally, these errors are zeros at the boundaries since those images are known and increase in the middle. Fig. 5 plots average SEs for images (top row) and tangents (bottom row). As these plots demonstrate clearly, our method vastly outperforms the other methods.

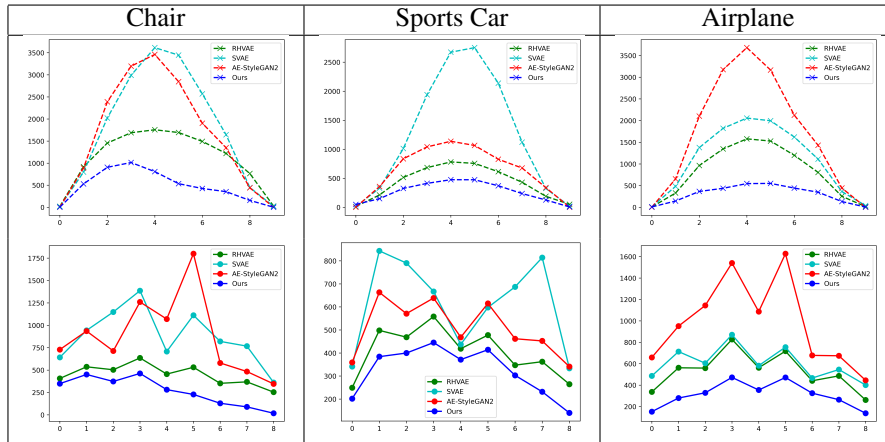


Figure 5: Summary statistics of squared errors average over 114 interpolated paths for each object. Top: Average SEs for interpolated points along all paths. Bottom: Average SEs for tangent vectors for all interpolated paths.

5.3 Image Denoising using Estimated Pose Manifolds

What are the practical uses of knowing the pose manifolds? One use is in denoising or cleaning corrupt images of objects. The basic idea is to take a given (noisy) image, map it into the latent space \mathbb{R}^d using Φ , and find the nearest point (using Euclidean distance) on the corresponding interpolated paths. We can then map this nearest point back to the image space and obtain a cleaner image. Fig. 6 shows some examples of this idea. The top row shows some images of the chair that have been corrupted using noisy patches and additive noise. When mapped back to the image space, the corresponding closest points on the pose manifold are shown as images in the bottom row.

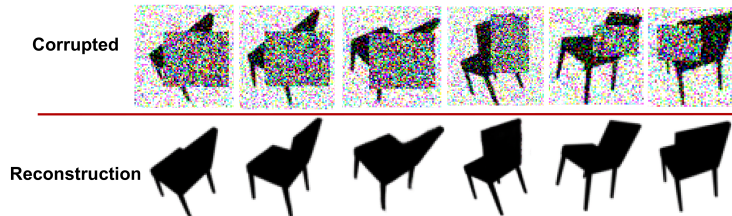


Figure 6: Replacing corrupted images (top) by their nearest neighbors on the learnt image manifold.

6 Conclusion and Discussion

This paper introduces a new approach for constructing latent spaces in generative models such as GANs and VAEs, focusing on preserving geometry and learning pose manifolds. The proposed method involves using Euler’s free elastica for interpolation within smaller latent spaces. These elastica use tangent spaces to facilitate nonlinear interpolation between data points. The approach achieves superior interpolation results by preserving pairwise distances between points and their tangent planes compared to the latest GANs and VAEs. This preservation of geometry, albeit only first

order, leads to improved performance both qualitatively and quantitatively. It achieves near-perfect simulation of videos of 3D rotations of objects given only boundary pose. The findings highlight the importance of accounting for the non-flat nature of latent space geometry.

References

- [1] Georgios Arvanitidis, Lars Kai Hansen, and Søren Hauberg. Latent space oddity on the curvature of deep generative models. In *Proceedings of International Conference on Learning Representations*, 2018.
- [2] Yoshua Bengio, Aaron Courville, and Pascal Vincent. Representation learning: A review and new perspectives. *IEEE Trans. Pattern Anal. Mach. Intell.*, 35:1798–1828, August 2013.
- [3] Clément Chadebec and Stephanie Allasonniere. A geometric perspective on variational autoencoders. In Alice H. Oh, Alekh Agarwal, Danielle Belgrave, and Kyunghyun Cho, editors, *Advances in Neural Information Processing Systems*, 2022. URL <https://openreview.net/forum?id=PBmJC6rDnR6>.
- [4] Aditya Chattopadhyay, Xi Zhang, David Paul Wipf, Himanshu Arora, and René Vidal. Learning graph variational autoencoders with constraints and structured priors for conditional indoor 3d scene generation. In *2023 IEEE/CVF Winter Conference on Applications of Computer Vision (WACV)*, pages 785–794, 2023. doi: 10.1109/WACV56688.2023.00085.
- [5] Johannes Chen, Johannes Ballé, Emilio Gómez, Marc’Aurelio Ranzato, and Alexander G Hauptmann. Variational image compression with a scale hyperprior. In *International Conference on Learning Representations*, 2017.
- [6] Tim R Davidson, Luca Falorsi, Nicola De Cao, Thomas Kipf, and Jakub M Tomczak. Hyperspherical variational auto-encoders. *arXiv preprint arXiv:1804.00891*, 2018.
- [7] Carl Doersch. Tutorial on variational autoencoders. In *arXiv preprint arXiv:1606.05908*, 2016.
- [8] David L. Donoho and Carrie Grimes. Hessian eigenmaps: Locally linear embedding techniques for high-dimensional data. *Proceedings of the National Academy of Sciences*, 100(10):5591–5596, 2003.
- [9] Ian Goodfellow, Jean Pouget-Abadie, Mehdi Mirza, Bing Xu, David Warde-Farley, Sherjil Ozair, Aaron Courville, and Yoshua Bengio. Generative adversarial networks. *Communications of the ACM*, 63(11): 139–144, 2020.
- [10] U. Grenander, A. Srivastava, and M. I. Miller. Asymptotic performance analysis of bayesian object recognition. *IEEE Transactions on Information Theory*, 46(4):1658–66, 2000.
- [11] Ligong Han, Sri Harsha Musunuri, Martin Renqiang Min, Ruijiang Gao, Yu Tian, and Dimitris Metaxas. Ae-stylegan: Improved training of style-based auto-encoders. In *Proceedings of the IEEE/CVF Winter Conference on Applications of Computer Vision*, pages 3134–3143, 2022.
- [12] Martin Heusel, Hubert Ramsauer, Thomas Unterthiner, Bernhard Nessler, and Sepp Hochreiter. Gans trained by a two time-scale update rule converge to a local nash equilibrium. *Advances in neural information processing systems*, 30, 2017.
- [13] Hanwen Jiang, Zhenyu Jiang, Kristen Grauman, and Yuke Zhu. Few-view object reconstruction with unknown categories and camera poses. *arXiv preprint arXiv:2212.04492*, 2022.
- [14] Tero Karras, Timo Aila, Samuli Laine, and Jaakko Lehtinen. Progressive growing of gans for improved quality, stability, and variation. In *International Conference on Learning Representations*, 2018.
- [15] Tero Karras, Samuli Laine, and Timo Aila. A style-based generator architecture for generative adversarial networks. In *Conference on Computer Vision and Pattern Recognition*, pages 4401–4410, 2019.
- [16] Tero Karras, Miika Aittala, Janne Hellsten, Samuli Laine, Jaakko Lehtinen, and Timo Aila. Training generative adversarial networks with limited data. *Advances in neural information processing systems*, 33: 12104–12114, 2020.
- [17] Tero Karras, Samuli Laine, Miika Aittala, Janne Hellsten, Jaakko Lehtinen, and Timo Aila. Analyzing and improving the image quality of stylegan. In *Proceedings of the IEEE/CVF conference on computer vision and pattern recognition*, pages 8110–8119, 2020.
- [18] Hiroharu Kato, Yoshitaka Ushiku, and Tatsuya Harada. Neural 3d mesh renderer. In *Proceedings of the IEEE conference on computer vision and pattern recognition*, pages 3907–3916, 2018.

- [19] Diederik P Kingma and Max Welling. Auto-encoding variational bayes. *arXiv preprint arXiv:1312.6114*, 2013.
- [20] Line Kühnel, Tom Fletcher, Sarang Joshi, and Stefan Sommer. Latent space geometric statistics. In *Pattern Recognition. ICPR International Workshops and Challenges*, pages 163–178, Cham, 2021. Springer International Publishing.
- [21] Anders Linnér. Existence of free nonclosed euler-bernoulli elastica. *Nonlinear Analysis: Theory, Methods & Applications*, 21(8):575–593, 1993. ISSN 0362-546X.
- [22] Miaomiao Liu, Xuming He, and Mathieu Salzmann. Geometry-aware deep network for single-image novel view synthesis. In *Proceedings of the IEEE Conference on Computer Vision and Pattern Recognition*, pages 4616–4624, 2018.
- [23] W. MIO, A. SRIVASTAVA, and E. KLASSEN. Interpolations with elasticae in euclidean spaces. *Quarterly of Applied Mathematics*, 62(2):359–378, 2004. ISSN 0033569X, 15524485. URL <http://www.jstor.org/stable/43638590>.
- [24] D. Mumford. Elastica and computer vision. page 491–506, 1994.
- [25] Phong Nguyen, Animesh Karnewar, Lam Huynh, Esa Rahtu, Jiri Matas, and Janne Heikkila. Rgb-d-net: Predicting color and depth images for novel views synthesis. In *2021 International Conference on 3D Vision (3DV)*, pages 1095–1105. IEEE, 2021.
- [26] Alec Radford, Luke Metz, and Soumith Chintala. Unsupervised representation learning with deep convolutional generative adversarial networks. *arXiv preprint arXiv:1511.06434*, 2015.
- [27] Danilo Jimenez Rezende and Shakir Mohamed. Stochastic backpropagation and approximate inference in deep generative models. In *International Conference on Machine Learning*, pages 1278–1286, 2015.
- [28] Sam T. Roweis and Lawrence K. Saul. Nonlinear dimensionality reduction by locally linear embedding. *Science*, 290(5500):2323–2326, 2000.
- [29] Hang Shao, Abhishek Kumar, and P. Thomas Fletcher. The riemannian geometry of deep generative models. *arXiv*, abs/1711.08014, 2017.
- [30] Ankita Shukla, Shagun Uppal, Sarthak Bhagat, Saket Anand, and Pavan Turaga. Geometry of deep generative models for disentangled representations. ICVGIP 2018, New York, NY, USA, 2020. Association for Computing Machinery.
- [31] Matthew Tancik, Vincent Casser, Xinchen Yan, Sabeek Pradhan, Ben Mildenhall, Pratul Srinivasan, Jonathan T. Barron, and Henrik Kretzschmar. Block-NeRF: Scalable large scene neural view synthesis. *arXiv*, 2022.

Supplementary Material

Title: Learning Pose Image Manifolds Using Geometry-Preserving GANs and Elasticae

Contents

1 Algorithms	1
2 Interpolated Paths	1
2.1 3D Chair Model	1
2.2 3D Sports Car Model	2
2.3 3D Airplane Model	5
2.4 3D Teapot Model	5

In this document, we provide some additional algorithms and results that could not be accommodated in the main paper. These results include algorithms to train and optimize the encoder E , detailed error analysis for each interpolated path, and examples of interpolated path between the original and rotated objects obtained from different poses. These additional results further demonstrate that our method leads to improved performance through both qualitative and quantitative evaluations.

1 Algorithms

In this section, we present procedures for training and optimizing encode E . Algorithm 1 provides details on how to preserve Pair-Wise Euclidean Distances, and Algorithm 2 on how to preserve Pair-wise Tangent Space Distances.

Algorithm 1 Pair-wise tangent space distances condition for optimizing encoder (E)

- 1: Given $I^p \in \mathbb{R}^{b \times c \times h \times l}$ and E .
 - 2: $D_{k,m}^{I^p} = \|\text{vec}(I_k^p) - \text{vec}(I_m^p)\|$, where $k, m = 1, \dots, b$, $w_k, w_m \in \mathbb{R}^d$, and $I_k^p, I_m^p \in \mathbb{R}^{c \times h \times l}$.
 - 3: $\tilde{w} = E(I^p) \in \mathbb{R}^{b \times d}$, $D_{k,m}^{\tilde{w}} = \|\tilde{w}_k - \tilde{w}_m\|$, where $\tilde{w}_k, \tilde{w}_m \in \mathbb{R}^d$.
 - 4: Compute $l_d(D^{\tilde{w}}, D^{I^p})$, where l_d is defined in Eqn. 1 in the main paper and do backpropagation.
 - 5: Update the weights in E .
-

2 Interpolated Paths

In this section, we provide examples of interpolated path between the original and rotated objects obtained from different poses. Furthermore, a comprehensive assessment of errors associated with each path is provided, through both quantitative and qualitative evaluations.

2.1 3D Chair Model

The example in Fig. 1 is the same as the example in Fig. 3 shown in the main paper, except that we add another row to show time-indexed image difference compared to the ground truth. Fig. 2(a) shows an interpolated path from a different pose, and Fig. 2(b), (c) show the corresponding quantifications of time-indexed squared errors in

Algorithm 2 Tangent plane condition for optimizing encoder E

- 1: Given $I^p \in \mathbb{R}^{b \times c \times h \times l}$, their neighboring points $\hat{I}^p \in \mathbb{R}^{n' \times c \times h \times l}$, and E .
 - 2: Expand I^p to $I^{*p} \in \mathbb{R}^{b \times n' \times c \times h \times l}$, where each of the n' columns is a replicate of I^p .
 - 3: Stack the neighboring points \hat{I}^p onto I^p , which yields a larger matrix denoted as $I'^p \in \mathbb{R}^{b \times n' \times c \times h \times l}$.
 - 4: Construct tangent plane in image space as $T^{I^p} = I'^p - I^{*p}$.
 - 5: Reshape the size of T^{I^p} from $\mathbb{R}^{b \times n' \times c \times h \times l}$ to $\mathbb{R}^{b \times n' \times chl}$, and compute the projection matrix for tangent plane T^{I^p} as $\mathcal{P}_k^{T^{I^p}} = (T_k^{I^p})^T T_k^{I^p}$, where $k = 1, \dots, b$, and $T_k^{I^p} \in \mathbb{R}^{n' \times chl}$.
 - 6: Compute pair-wise distance matrix $D_{k,m}^{T^{I^p}} = \|\mathcal{P}_k^{T^{I^p}} - \mathcal{P}_m^{T^{I^p}}\|_f$, where $k, m = 1, \dots, b$, $\mathcal{P}_k^{T^{I^p}}, \mathcal{P}_m^{T^{I^p}} \in \mathbb{R}^{chl \times chl}$, and $\|\cdot\|_f$ is the Frobenius Norm.
 - 7: $\tilde{w} = E(I^p) \in \mathbb{R}^{b \times d}$, then expand \tilde{w} to $\tilde{W}^* \in \mathbb{R}^{b \times n' \times d}$, where each of the n' columns is a replicate of w . Besides, compute $\tilde{W}' = E(I'^p) \in \mathbb{R}^{b \times n' \times d}$.
 - 8: Construct tangent plane in latent space as $T^{\tilde{w}} = \tilde{W}' - \tilde{W}^*$.
 - 9: Compute projection matrix for tangent plane $T^{\tilde{w}}$ as $\mathcal{P}_k^{T^{\tilde{w}}} = (T_k^{\tilde{w}})^T T_k^{\tilde{w}}$, where $k = 1, \dots, b$.
 - 10: Compute pair-wise distance matrix $D_{k,m}^{T^{\tilde{w}}} = \|\mathcal{P}_k^{T^{\tilde{w}}} - \mathcal{P}_m^{T^{\tilde{w}}}\|_f$, where $k, m = 1, \dots, b$, $\mathcal{P}_k^{T^{\tilde{w}}}, \mathcal{P}_m^{T^{\tilde{w}}} \in \mathbb{R}^{d \times d}$, and $\|\cdot\|_f$ is the Frobenius Norm.
 - 11: Compute $l_d(D^{T^{I^p}}, D^{T^{\tilde{w}}})$, where l_d is defined in Eqn. 1 in the main paper and do backpropagation.
 - 12: Update the weights in E .
-

the image space and the tangents. We can see that the interpolated paths obtained by our method are close to the ground truth, while the other methods severely distort intermediate images in multiple ways.

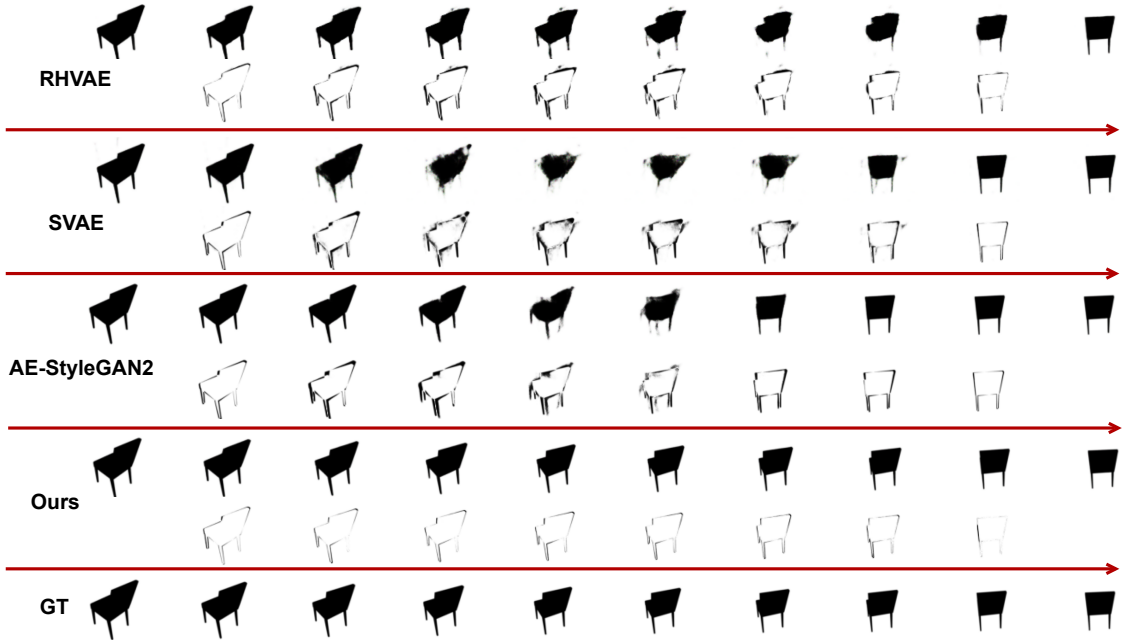
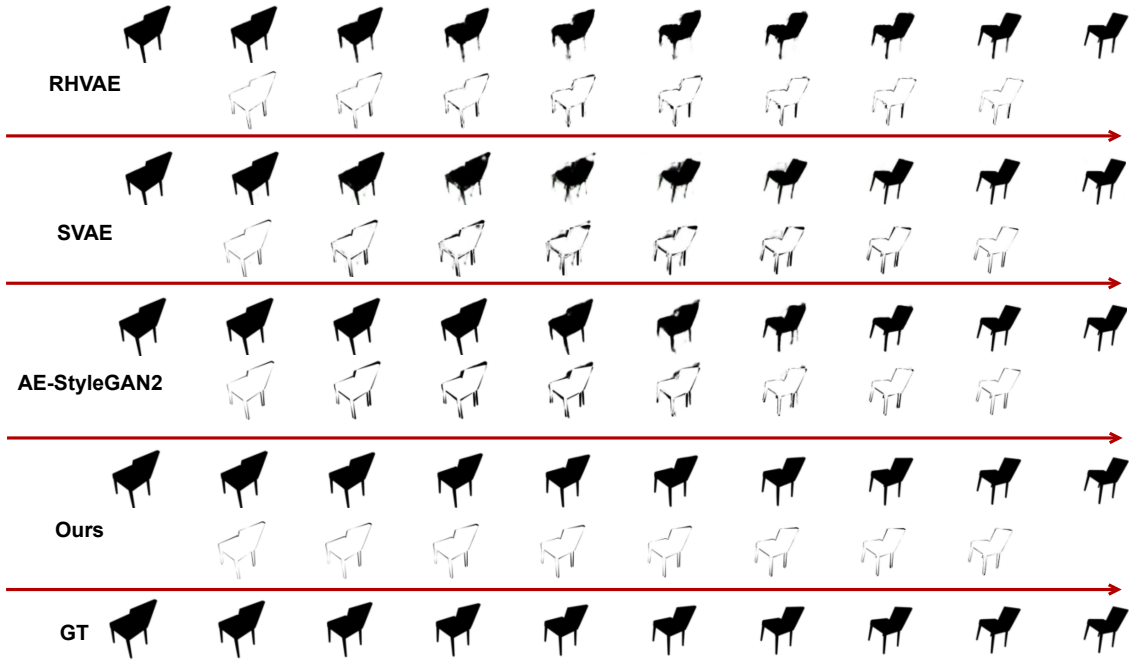


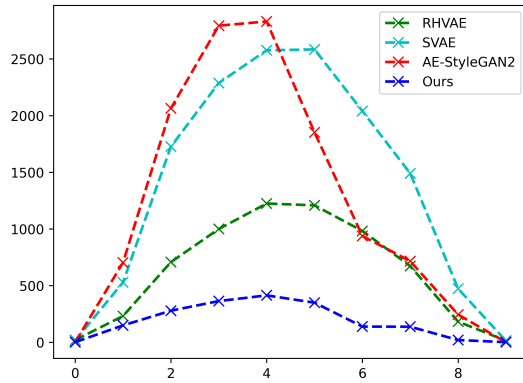
Figure 1: Each of first row shows an interpolated path between the original pose (leftmost) and the rotated pose (rightmost) using the corresponding methods, and each of second rows shows the time-indexed image difference compared to the ground truth. The rotation angle between the two pose is 40 degrees.

2.2 3D Sports Car Model

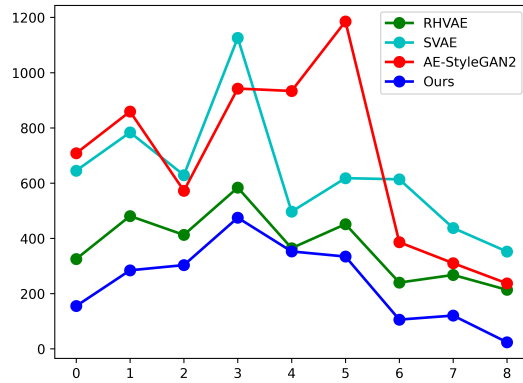
Fig. 3(a) shows an interpolated path from a different pose, and Fig. 3(b), (c) show the corresponding quantifications of time-indexed squared errors in the image space and the tangents. We can see that the interpolated paths obtained by our method are close to the ground truth, while the other methods severely distort intermediate images in multiple ways.



(a) Interpolated path visualization with its corresponding image difference compared to the ground truth



(b) Time-indexed squared errors

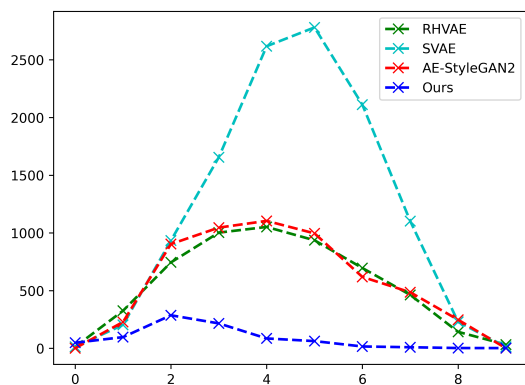


(c) Tangents squared errors

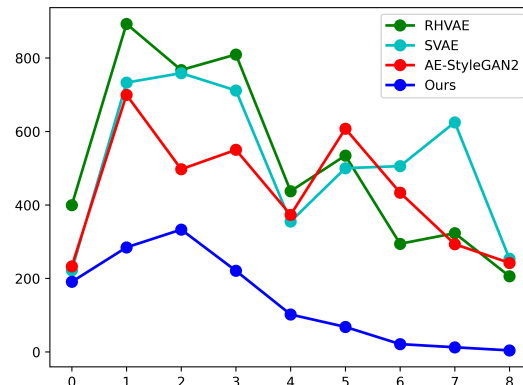
Figure 2: (a): Each of first row shows an interpolated path between the original pose (leftmost) and the rotated pose (rightmost) using the corresponding methods, and each of second rows shows the time-indexed image difference compared to the ground truth. The rotation angle between the two pose is 30 degrees. (b), (c): Plots of time-indexed squared errors in the image space (left) and the tangents (right) for different methods.



(a) Interpolated path visualization with its corresponding image difference compared to the ground truth



(b) Time-indexed squared errors



(c) Tangents squared errors

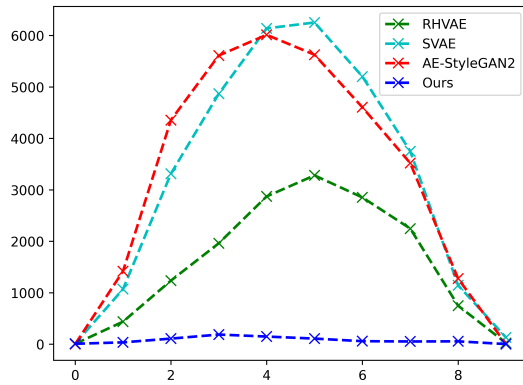
Figure 3: (a): Each of first row shows an interpolated path between the original pose (leftmost) and the rotated pose (rightmost) using the corresponding methods, and each of second rows shows the time-indexed image difference compared to the ground truth. The rotation angle between the two pose is 30 degrees. (b), (c): Plots of time-indexed squared errors in the image space (left) and the tangents (right) for different methods.

2.3 3D Airplane Model

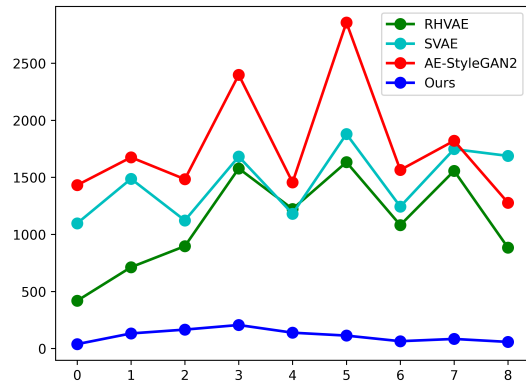
Fig. 4(a) shows an interpolated path from a different pose, and Fig. 4(b), (c) show the corresponding quantifications of time-indexed squared errors in the image space and the tangents. We can see that the interpolated paths obtained by our method are close to the ground truth, while the other methods severely distort intermediate images in multiple ways.



(a) Interpolated path visualization with its corresponding image difference compared to the ground truth



(b) Time-indexed squared errors



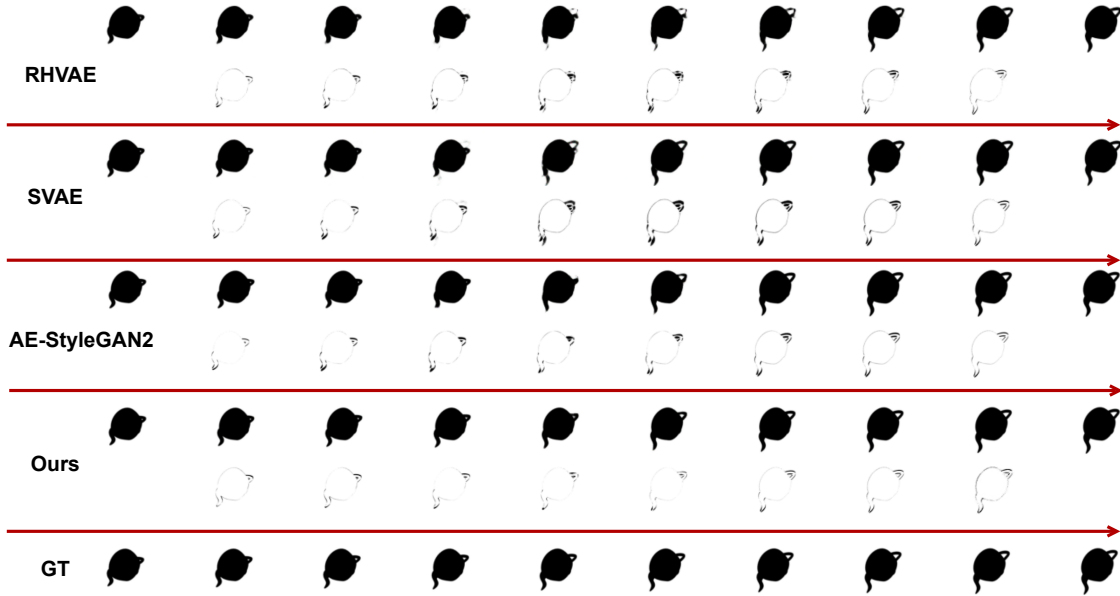
(c) Tangents squared errors

Figure 4: (a): Each of first row shows an interpolated path between the original pose (leftmost) and the rotated pose (rightmost) using the corresponding methods, and each of second rows shows the time-indexed image difference compared to the ground truth. The rotation angle between the two pose is 30 degrees. (b), (c): Plots of time-indexed squared errors in the image space (left) and the tangents (right) for different methods.

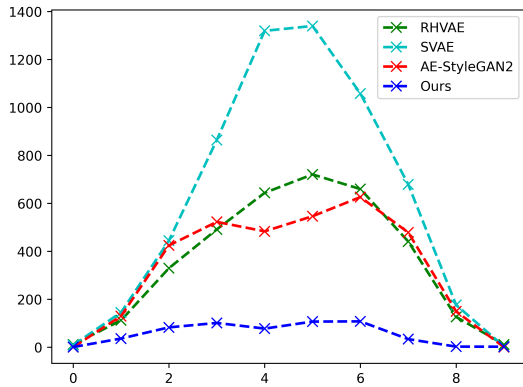
2.4 3D Teapot Model

We provide two examples of 3D Teapot Model here. Fig. 5(a) shows an interpolated path, and Fig. 5(b), (c) show the corresponding quantifications of time-indexed squared errors in the image space and the tangents. Fig. 6(a) shows an interpolated path from a different pose, and Fig. 6(b), (c) show the corresponding quantifications of time-indexed squared errors in the image space and the tangents. We can see that the interpolated paths obtained by

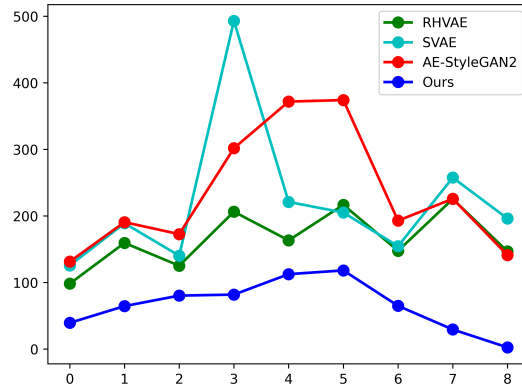
our method are close to the ground truth, while the other methods severely distort intermediate images in multiple ways.



(a) Interpolated path visualization with its corresponding image difference compared to the ground truth

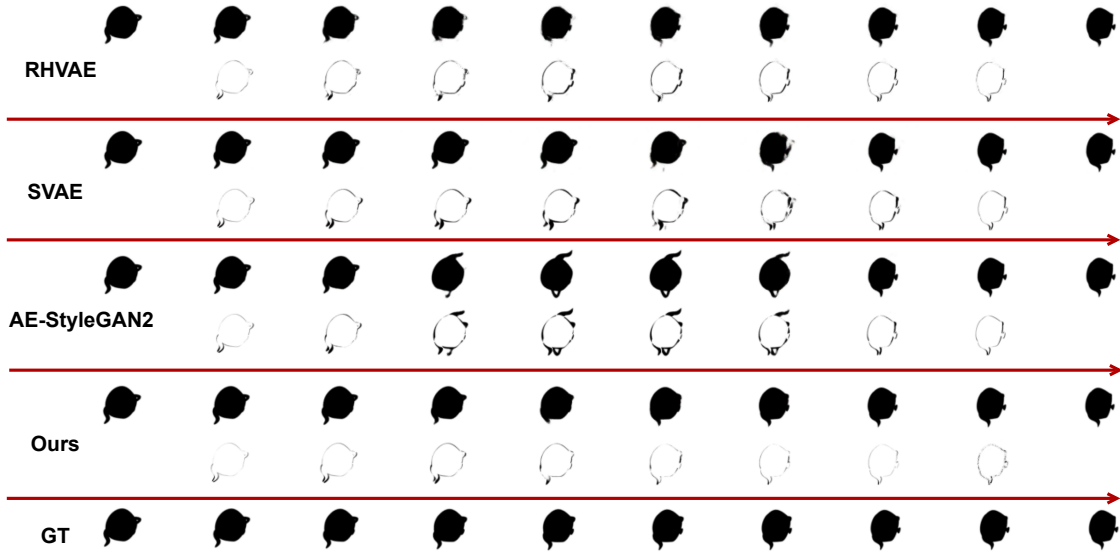


(b) Time-indexed squared errors

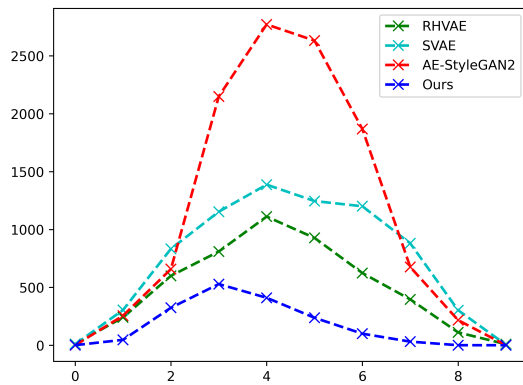


(c) Tangents squared errors

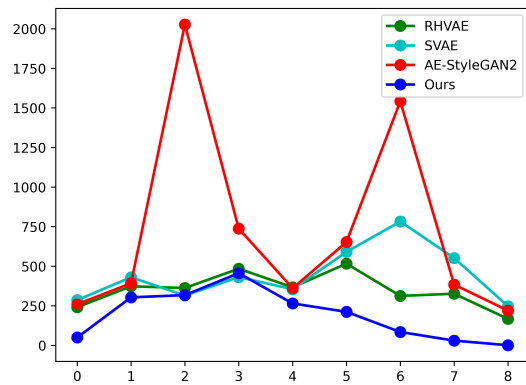
Figure 5: (a): Each of first row shows an interpolated path between the original pose (leftmost) and the rotated pose (rightmost) using the corresponding methods, and each of second rows shows the time-indexed image difference compared to the ground truth. The rotation angle between the two pose is 25 degrees. (b), (c): Plots of time-indexed squared errors in the image space (left) and the tangents (right) for different methods.



(a) Interpolated path visualization with its corresponding image difference compared to the ground truth



(b) Time-indexed squared errors



(c) Tangents squared errors

Figure 6: (a): Each of first row shows an interpolated path between the original pose (leftmost) and the rotated pose (rightmost) using the corresponding methods, and each of second rows shows the time-indexed image difference compared to the ground truth. The rotation angle between the two pose is 25 degrees. (b), (c): Plots of time-indexed squared errors in the image space (left) and the tangents (right) for different methods.